Biosensors and Bioelectronics 195 (2022) 113620

Contents lists available at ScienceDirect

Biosensors and Bioelectronics

journal homepage: www.elsevier.com/locate/bios

Ti_3C_2-MXene decorated with nanostructured silver as a dual-energy acceptor for the fluorometric neuron specific enolase detection

Ashish Kalkal [a], Sachin Kadian [b], Sumit Kumar [c], Gaurav Manik [b], Prosenjit Sen [d], Saurabh Kumar [d,e,**], Gopinath Packirisamy [a,f,*]

[a] Nanobiotechnology Laboratory, Department of Biosciences and Bioengineering, Indian Institute of Technology Roorkee, Uttarakhand, 247667, India
[b] Department of Polymer and Process Engineering, Indian Institute of Technology Roorkee, Uttarakhand, 247667, India
[c] Department of Research and Innovations, Division of Research and Development, Lovely Professional University, Jalandhar, Punjab, 144411, India
[d] Centre for Nano Science and Engineering (CeNSE), Indian Institute of Science Bengaluru, Karnataka, 560012, India
[e] Department of Medical Devices, National Institute of Pharmaceutical Education and Research Guwahati, Assam, 781101, India
[f] Centre for Nanotechnology, Indian Institute of Technology Roorkee, Uttarakhand, 247667, India

ARTICLE INFO

Keywords:
Energy transfer
Ti_3C_2-MXene
Graphene quantum dots (GQDs)
Fluorescent biosensor
Neuron-specific enolase (NSE)

ABSTRACT

Nanohybrids of two-dimensional (2D) layered materials have shown fascinating prospects towards the fabrication of highly efficient fluorescent immunosensor. In this context, a nanohybrid of ultrathin Ti_3C_2-MXene nanosheets and silver nanoparticles (Ag@Ti_3C_2-MXene) has been reported as a dual-energy acceptor for ultra-high fluorescence quenching of protein-functionalized graphene quantum dots (anti-NSE/amino-GQDs). The Ti_3C_2-MXene nanosheets are decorated with silver nanoparticles (AgNPs) to obsolete the agglomeration and restacking through a one-pot direct reduction method wherein the 2D Ti_3C_2-MXene nanosheets acted both as a reducing agent and support matrix for AgNPs. The as-prepared nanohybrid is characterized by various techniques to analyze the optical, structural, compositional, and morphological parameters. The quenching efficiency and energy transfer capability between the anti-NSE/amino-GQDs (donor) and Ag@Ti_3C_2-MXene (acceptor) have been explored through steady state and time-resolved spectroscopic studies. Interestingly, the Ag@Ti_3C_2-MXene nanohybrid exhibits better quenching and energy transfer efficiencies in contrast to bare Ti_3C_2-MXene, AgNPs and previously reported AuNPs. Based on optimized donor-acceptor pair, a fluorescent turn-on biosensing system is constructed that revealed improved biosensing characteristics compared to Ti_3C_2-MXene, graphene and AuNPs for the detection of neuron-specific enolase (NSE), including higher sensitivity (~771 mL ng^{-1}), broader linear detection range (0.0001–1500 ng mL^{-1}), better LOD (0.05 pg mL^{-1}), and faster response time (12 min). Besides, remarkable biosensing capability has been observed in serum samples, with fluorescence recovery of ~98%.

1. Introduction

A rapid accession in the exploration of zero-dimensional (0D) and two-dimensional (2D) based nanohybrid materials comprising derivatives of graphene, metal nanoparticles, transition metal oxides, dichalcogenides, including carbides, nitrides, and carbonitrides has shown a multifold rise in the field of bio and nanoelectronics engineering (Anasori et al., 2017; Chauhan et al., 2020; Kalkal et al., 2021c; Kumar et al. 2016, 2018a, Kumar et al., 2019a; Liu et al., 2017; Peng et al., 2016). These advanced materials possess exceptional optical, mechanical, electronic, and physicochemical properties. Owing to these properties, their utilization has shown a well-proven scope in plenty of applications, especially energy conversion (Kumar et al., 2019b; Sun et al., 2017), supercapacitor (Zhou et al., 2020), biomedical (Huang et al., 2018), water purification (Pandey et al., 2018), and biosensing (Kumar et al., 2018a; Pradhan et al., 2021a). Moreover, in the last decade, 2D layered materials delivered an extraordinary impact in the field of fluorescent biosensors, wherein efficient donor-acceptor pairs are being explored to obtain enhanced energy transfer rates in view of achieving improved analytical performance (Neema et al., 2020; Peng

* Corresponding author. Nanobiotechnology Laboratory, Department of Biosciences and Bioengineering, Indian Institute of Technology Roorkee, Uttarakhand, 247667, India.
** Corresponding author. Centre for Nano Science and Engineering (CeNSE), Indian Institute of Science Bengaluru, Karnataka, 560012, India.
E-mail addresses: sau2203@gmail.com (S. Kumar), genegopi@gmail.com, gopi@bt.iitr.ac.in (G. Packirisamy).

https://doi.org/10.1016/j.bios.2021.113620
Received 27 May 2021; Received in revised form 18 August 2021; Accepted 6 September 2021
Available online 16 September 2021

et al., 2019; Tian et al., 2017; Zhu et al., 2019).

In this direction, quantum dots, including molybdenum disulfide (MOS_2), carbon dots (CDs), graphene quantum dots (GQDs), etc., have immensely evolved as energy donor species due to their unusual optical and electronic properties (Bhatnagar et al., 2016; Kadian et al., 2019; Kalkal et al., 2021a; Shao et al., 2019; Swaminathan et al., 2017). These quantum dots provide good biocompatibility, broad excitation spectra, good water solubility, tunable emission spectra, and intense fluorescence with long-term photostability (Kalkal et al. 2020, 2021b). On the other hand, 0D and 2D nanomaterials, including metal nanoparticles (gold and silver nanoparticles (Au and Ag NPs), graphene and its derivatives (reduced graphene oxide (RGO), graphene oxide (GO)) have been deployed as energy acceptor species in the development of fluorescent biosensors (Ghosh and Chattopadhyay, 2015; Neema et al., 2020). Conforming to this, Amjadi et al. demonstrated the fluorescent turn-on sensing probe for the detection of cysteine that utilizes CDs and AgNPs as donor-acceptor pair (Amjadi et al., 2015). In our previous work, we recently reported the development of a fluorescent biosensor for NSE detection based on AuNPs and amine-functionalized nitrogen-doped GQDs (Kalkal et al., 2020). Conversely, Bhatnagar et al. fabricated an immunosensor utilizing GQDs and graphene as energy donor-acceptor pair for detecting cardiac troponin I (CTnI) biomarker. (Bhatnagar et al., 2016).

However, it has been predicted that dispersed metal nanoparticles may tend to agglomerate in solution due to the Brownian motion of suspended nanoparticles, forming larger clusters having a smaller surface area that may inhibit the energy transfer efficiency and quenching capabilities (Mahdavi et al., 2019; Tilaki et al., 2006). Besides, 2D layered nanomaterials have a tendency to restack due to strong van der Waals forces between the adjacent nanosheets that may further influence the biosensing parameters (Atif and Inam, 2016; Cha et al., 2016; He et al., 2019). These problems might be overcome by preparing a 0D and 2D-based nanohybrid material that can work as a dual-energy acceptor and facilitate in improving the energy transfer efficiency along with biosensing parameters. In that, 2D layered nanomaterial can help in inhibiting the Brownian motion of metal nanoparticles by acting as a support matrix, thereby avoiding the inherent agglomeration. Additionally, the restacking among the 2D nanosheets can be inhibited by incorporating the 0D nanoparticles that help in generating the interlayer spacing among layered nanosheets (Kalali et al., 2020; Torres-Mendieta et al., 2016). In this context, Kumar et al. utilized the RGO nanosheets as the support matrix to reduce the agglomeration by inhibiting the Brownian motion of nanostructured metal oxide. The resultant nanohybrid-based sensing platform exhibited superior biosensing parameters, including higher sensitivity and broader linear detection range (Kumar et al., 2018a; Kumar and Kalkal, 2021). However, in case of graphene-based 2D nanomaterials, the decoration of 0D nanomaterials can occur only on edge and defect sites of graphene nanosheets (Bellunato et al., 2016; Vedala et al., 2011). Besides, chemically synthesized graphene (RGO) requires an additional reducing agent for *in-situ* decoration or an additional step for *ex-situ* decoration of 0D nanomaterial on RGO nanosheets (Cui et al., 2013; Ikram et al., 2020; Su et al., 2018). Moreover, the conventional graphene-based 2D layered nanomaterials possess low-hydrophilicity, inadequate surface terminated functionality, difficulty in functionalization that may influence the intrinsic properties and fluorescent biosensing applications of graphene-based layered materials.

In the view of foregoing, a new and emerging material named MXene having the general formula of $M_{n+1}X_nT_x$ (M represents a transition metal, X can be nitrogen and/or carbon, and T_x denotes surface functionalization) has attracted enormous consideration for the biosensing applications (Ghidiu et al., 2014; Khazaei et al., 2013; Naguib et al., 2011). Among them, Ti_3C_2-MXene is known for its metallic conductivity, super hydrophilicity, broad and strong absorption, polar surfaces, large surface area, which make them viable for electrochemical as well as fluorescent biosensors (Anasori et al., 2017; Kumar et al., 2018b; Zhang et al., 2018). The ultrathin Ti_3C_2-MXene sheets terminated with oxygen and hydroxyl groups facilitate the material to communicate with a large number of biomolecules via hydrogen bonds, coordination bonds, van der Waals forces, and electrostatic interactions. Moreover, Ti_3C_2-MXene sheets exhibit wideband absorption in UV–vis region over its large surface area in conjunction with long-range electron and energy transferability, which enable the Ti_3C_2-MXene to become a prominent energy acceptor or quencher species (Shi et al., 2019; Zhang et al., 2018). Despite great potential, it has been observed that Ti_3C_2-MXene as a fluorescence quencher/energy acceptor is not explored much, and only a few attempts have been made in this direction (Peng et al., 2019; Shi et al., 2019; Zhang et al., 2018; Zhu et al., 2019). Unlike graphene, Ti_3C_2-MXene offers excellent aqueous solubility, superior surface terminated functionality, larger surface area, and better biocompatibility, preferable in the fabrication of efficient fluorescent biosensors (Song et al., 2020; Soomro et al., 2020). Besides, the self-reducing capability of Ti_3C_2-MXene exempt the requirement of additional reducing agent for decorating 0D nanomaterial on Ti_3C_2-MXene nanosheets.

Small cell lung cancer (SCLC) a distinct histological subgroup of lung cancer, is associated with poor prognosis, strong predilection for early metastasis, and exceptionally high proliferative rate (Rudin et al., 2021). SCLC is the most hostile form of lung cancer, accounting for around 15–20% of new cases. Besides, it is marked by acquired chemoresistance and high sensitivity to radiation and chemotherapy, and therefore difficult to cure (Jackman and Johnson, 2005). It can be life-threatening and metastasize to other body parts if not diagnosed at an initial stage. Therefore, there is an increased demand for SCLC's rapid and early detection, lowering the mortality rate. In this context, neuron specific enolase (NSE) is reported as an efficient biomarker for monitoring therapeutic treatment efficacy, disease progression, assessing tumor burden, and early diagnosis in view of its higher secretion rate (Amani et al., 2018; Han et al., 2012; Xiao et al., 2017). For healthy persons, the NSE concentration in serum can be up to 12–13 ng mL^{-1} while SCLC patients have this concentration more than 35 ng mL^{-1} (Harding et al., 1990; Kalkal et al., 2020; Shibayama et al., 2001). Quantitative detection of NSE in serum can be an exciting alternative for monitoring and clinical diagnosis of SCLC.

We report results of the studies relating to the fabrication and utilization of Ag@Ti_3C_2-MXene nanohybrid as a dual-energy acceptor for the development of a rapid, label-free, and highly sensitive fluorescent biosensor. The fabricated biosensor rely on the efficient trade-off between the donor (anti-NSE/amino-GQDs) and acceptor (Ag@Ti_3C_2-MXene) pair following the nanosurface energy transfer (NSET) mechanism. The Ag@Ti_3C_2-MXene nanohybrid based biosensor reveals improved biosensing characteristics in standard and spiked serum samples for NSE detection compared to bare Ti_3C_2-MXene, classic graphene and earlier reported AuNPs (Kalkal et al., 2020).

2. Materials and methods

2.1. Preparation of Ag@Ti_3C_2-MXene nanohybrid

Ag@Ti_3C_2-MXene nanohybrid has been obtained via the one-pot direct reduction of aqueous $AgNO_3$ salt to AgNPs onto Ti_3C_2-MXene nanosheets. In this process, the 2D Ti_3C_2-MXene nanosheets acted both as a reducing agent and support matrix for AgNPs. Initially, 84.93 mg of $AgNO_3$ is dispersed in 50 mL of deionized water through a vortex mixture to provide the 10 mM aqueous solution. On the other hand, 200 mg of powdered Ti_3C_2-MXene (supporting **information, S3**) is suspended in 20 mL of distilled water followed by ultrasonication for 30 min to provide the uniformly dispersed stock concentration (10 mg mL^{-1}). After that, 5 mL of dispersed Ti_3C_2-MXene with diluted concentrations (0.5, 1, 2, 5 mg mL^{-1}) is added in a dropwise manner to the above-prepared $AgNO_3$ aqueous solution and continued stirring for 60 min. Fig. S1 shows the images of obtained Ag@Ti_3C_2-MXene nanohybrid

solution with different Ti_3C_2-MXene concentrations. The obtained solution of Ag@Ti_3C_2-MXene nanohybrid is centrifuged at 10,000 rpm and washed multiple times to remove the impurities. Finally, the resultant solution is vacuum dried to obtain the powdered Ag@Ti_3C_2-MXene nanohybrid.

2.2. Protein functionalization of amino graphene quantum dots (anti-NSE/amino-GQDs)

The hydrothermally synthesized amino-GQDs (supporting **information, S4**) are protein functionalized using the standard EDC-NHS coupling chemistry (Kalkal et al., 2020; Kumar et al., 2018a). To activate the carboxyl groups of monoclonal anti-NSE antibody, a solution containing 250 μL of anti-NSE (50 μg mL^{-1}), 125 μL of NHS (0.05 M), and 125 μL of EDC (0.2 M) is prepared and allowed to incubate for 30 min at room temperature. The activated anti-NSE antibody solution is mixed with an equal volume (500 μL, 1:1 v/v) of amino-GQDs solution (20 μg mL^{-1}) and incubated in a humid chamber for about 2 h. After that, the anti-NSE/amino-GQDs solution is ultra-centrifuged and washed with deionized water to remove the unbound antibodies. The protein functionalized GQDs are characterized by zeta potential, FTIR, and UV–vis techniques (supporting **information (S6), Figs. S2c–e).**

2.3. Design of fluorescent biosensor

The detection of target cancer biomarker is carried out in 50 mM phosphate-buffered saline (PBS) solution (pH 7.4) at room temperature by recording the fluorescence emission spectra. Here, 500 μL of protein-functionalized amino-GQDs energy donor is mixed with 200 μL of Ag@Ti_3C_2-MXene nanohybrid (50 μg mL^{-1}) energy acceptor. After that, 50 μL of distinct NSE concentrations (0.0001–1500 ng mL^{-1}) is added to the donor-acceptor mixture (anti-NSE/amino-GQDs/Ag@Ti_3C_2-MXene) and allowed to incubate for an interval of 12 min. Consequently, the alterations in fluorescence intensity are computed at the excitation wavelength of 360 nm with the increasing NSE antigen concentration in the resultant mixture. The selectivity studies of the fabricated biosensor have been performed by adding fixed concentration (50 μL, 0.1 ng mL^{-1}) of various interfering biomarkers into anti-NSE/amino-GQDs/Ag@Ti_3C_2-MXene solution, followed by the measurement of corresponding emission spectra. The real sample analysis is performed in NSE spiked serum samples that are obtained from the hospital, Indian Institute of Technology Roorkee (IITR), after ethical approval by the Institutional Biosafety and Ethical Committee (BT/IHEC-IITR/2019/7525) (Pradhan et al., 2021b). 50 μL of serum samples spiked with different NSE concentrations (10, 20, 50, 100, and 150 ng mL^{-1}) is added into the optimized donor-acceptor solution (anti-NSE/amino-GQDs/Ag@Ti_3C_2-MXene) to record the corresponding emission spectra as described above.

3. Results and discussion

3.1. Mechanism of proposed fluorescent biosensor

The working of the proposed anti-NSE/amino-GQDs/Ag@Ti_3C_2-MXene biosensor is elaborated in a three-step process, and a schematic representation of the plausible mechanism is illustrated in Fig. 1. The driving force behind any fluorescent biosensor is based on the fluorescent state (**ON/OFF**) of the fluorophore, irrespective of its nature. In the first step, the fluorescence intensity of synthesized donor species (anti-NSE/amino-GQDs) is recorded at an excitation wavelength of 360 nm, which emit intense blue fluorescence around 450 nm (**ON** state). Secondly, the optimized amount of anti-NSE/amino-GQDs are physically adsorbed on the surface of Ag@Ti_3C_2-MXene nanohybrid through non-covalent interactions, which leads to an abrupt fluorescence quenching owing to dipole-surface interactions (**OFF** state). The Ag@Ti_3C_2-MXene nanohybrid acts as a dual-quencher in a single system for ultra-

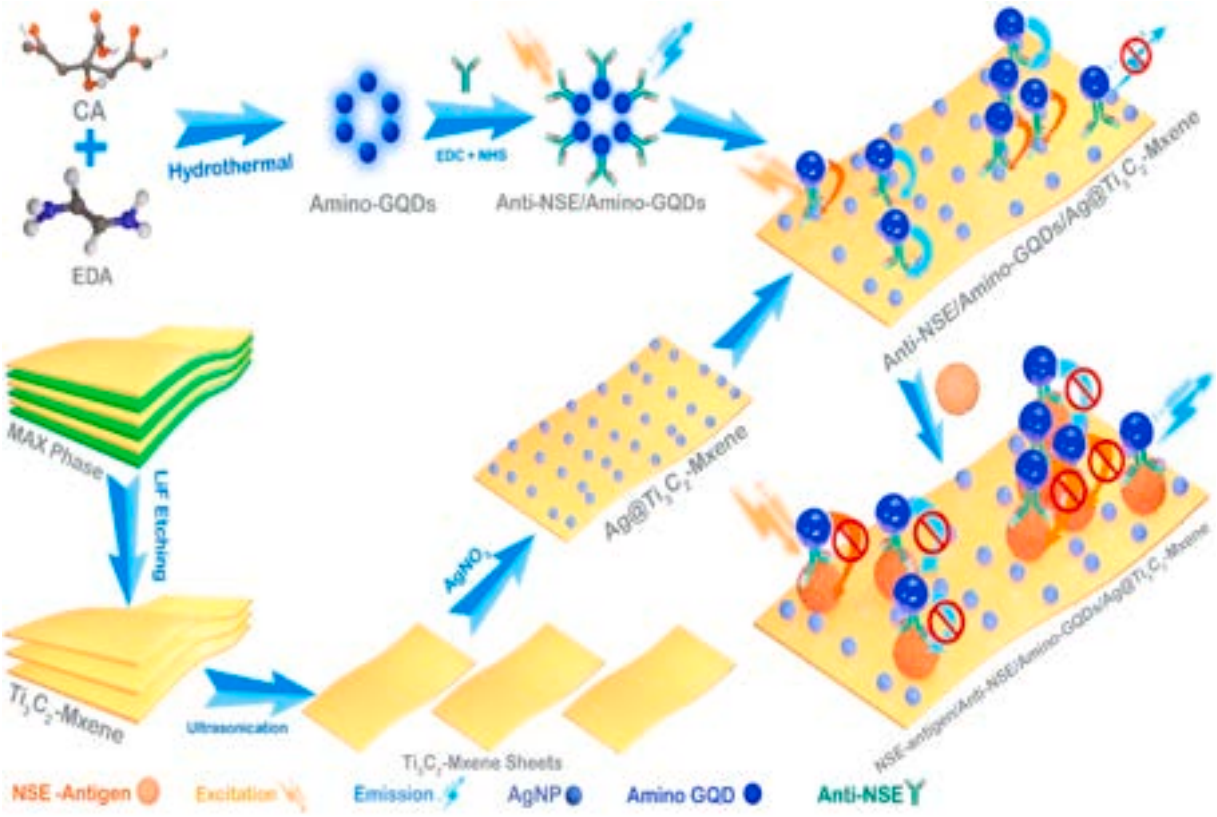

Fig. 1. Schematic illustration of anti-NSE/amino-GQDs/Ag@Ti_3C_2-MXene based biosensing platform for the fluorometric NSE detection.

high fluorescence quenching of donor species owing to their higher surface to volume ratio that enables effective energy transfer utilizing the concept of single-acceptor multiple-donor. In this context, the orange-colored arrows in Fig. 1 indicate the energy transfer to AgNPs from anti-NSE/amino-GQDs donor species. In contrast, energy transfer to Ti_3C_2-MXene nanosheets is shown with cyan-colored arrows. The 0D-2D complex of Ag@Ti_3C_2-MXene nanohybrid combines the benefit of both 0D AgNPs and 2D Ti_3C_2-MXene as individual energy acceptors. At last, the addition of the target antigen in the anti-NSE/amino-GQDs/Ag@Ti_3C_2-MXene biocomplex leads to specific immunocomplex (antigen-antibody) formation. Due to this, the fluorescence gets recovered (**ON** state) from the non-interacted anti-NSE/amino-GQDs donor as they detached from the Ag@Ti_3C_2-MXene nanohybrid surface due to the inferior non-covalent interactions. The recovered fluorescence from the donor species further relies on the added NSE concentration.

3.2. Characterizations of Ag@Ti_3C_2-MXene nanohybrid

3.2.1. Optical characterizations

The optical properties of synthesized Ti_3C_2-MXene and Ag@Ti_3C_2-MXene nanohybrid are identified from their corresponding colloidal solutions. The color of the synthesized Ag@Ti_3C_2-MXene nanohybrid complex appeared dark golden due to the reduction of $AgNO_3$ to AgNPs by Ti_3C_2-MXene nanosheets (Fig. S1). Besides, the validation of reduction has been studied through UV–vis spectroscopy (Fig. 2a), wherein initially a sharp absorption peak around 300 nm for $AgNO_3$ salt and a broad peak around 270 nm for Ti_3C_2-MXene is observed (Kumar et al., 2018b). A continuous decrement in $AgNO_3$ peak intensity and subsequently an increment in the intensity of AgNPs surface plasmon resonance (SPR) peak at 438 nm, with increasing concentrations of Ti_3C_2-MXene reflect the reduction and successful formation of Ag@Ti_3C_2-MXene nanohybrid (Pandey et al., 2018).

3.2.2. Structural and morphological characterizations

The structural characterizations of synthesized AgNPs, Ti_3C_2-MXene and Ag@Ti_3C_2-MXene nanohybrid are investigated via XRD analysis (Fig. 2b). The AgNPs exhibits four sharp crystalline peaks associated to (111), (200), (220), and (311) planes at 2θ angle 38.5°, 44.7°, 64.8°, and 77.7°, respectively (JCPDS card no. 040783) (Zou et al., 2016). In Ti_3C_2-MXene, a weak and broad peak at 2θ = 6.8 corresponding to (002) plane is observed, elucidating the formation of Ti_3C_2-MXene nanosheets (Kumar et al., 2018b). The spectrum of Ag@Ti_3C_2-MXene replicates the diffraction peaks of AgNPs and Ti_3C_2-MXene, indicating the nanohybrid formation. Interestingly, no peak shift has been observed in the spectrum of resultant nanohybrid that evince the decoration of AgNPs on the surface of Ti_3C_2-MXene nanosheets (Pandey et al., 2018).

The pivotal information such as surface chemical bonding, elemental composition, and the plausible direct reduction mechanism concerning

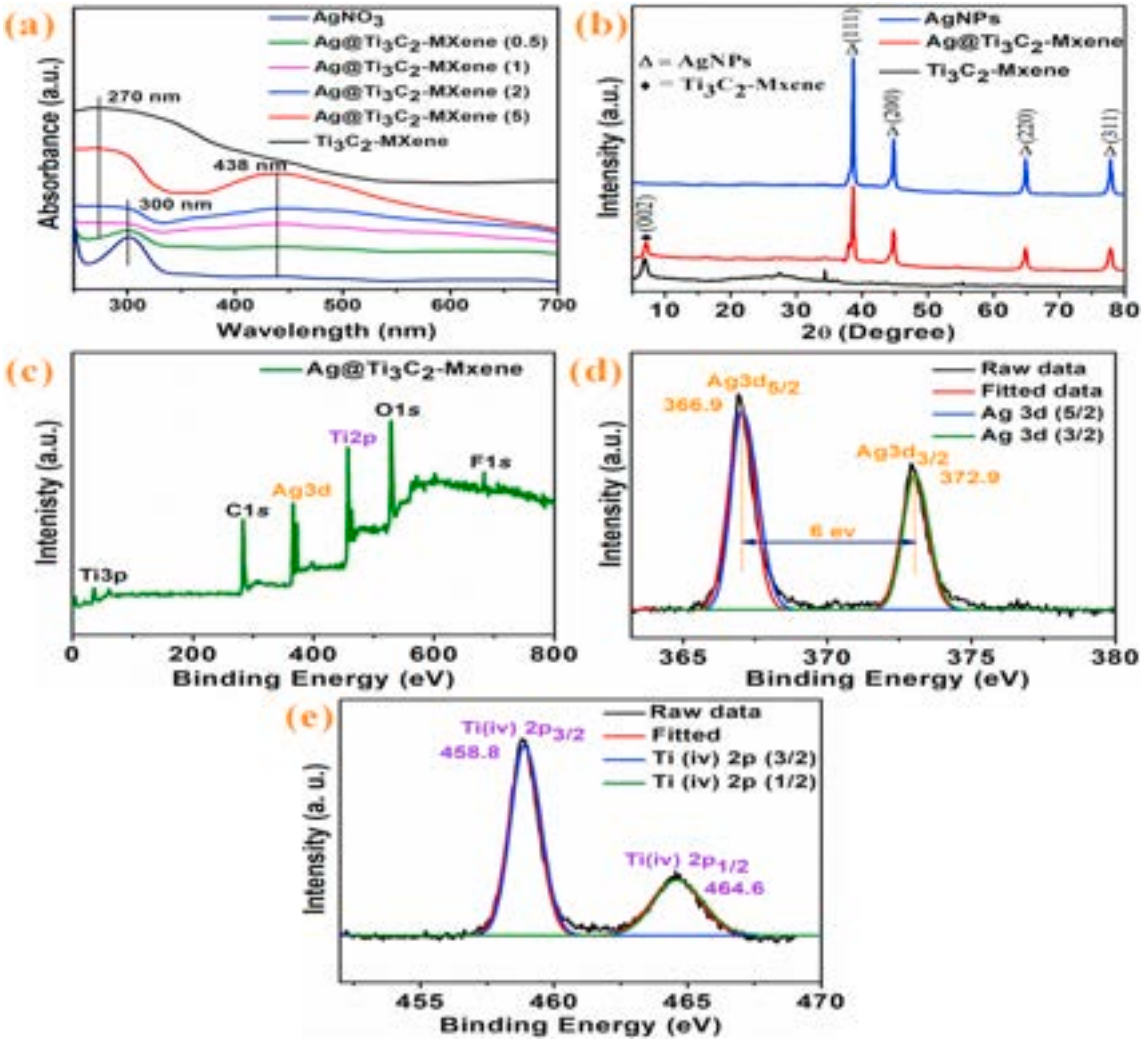

Fig. 2. **(a)** UV–vis absorption spectra of Ti_3C_2-MXene, Ag@Ti_3C_2-MXene nanohybrid with different concentrations of Ti_3C_2-MXene (0.5, 1, 2, 5 mg mL^{-1}), and $AgNO_3$ salt respectively; **(b)** Diffraction pattern of AgNPs, Ag@Ti_3C_2-MXene nanohybrid, bare Ti_3C_2-MXene; **(c)** Full scan XPS profile of Ag@Ti_3C_2-MXene nanohybrid; **(d)** Deconvoluted Ag 3d spectra for Ag@Ti_3C_2-MXene nanohybrid; **(e)** Deconvoluted Ti 2p spectra for Ag@Ti_3C_2-MXene nanohybrid.

Ag@Ti_3C_2-MXene nanohybrid are investigated through XPS analysis. The full scan XPS spectra of the synthesized Ag@Ti_3C_2-MXene nanohybrid reveal the existence of C 1s, Ag 3d, O 1s, Ti 2p, Ti 3p, and F1s components (Fig. 2c). The detailed chemical bonding analysis of Ag and Ti have been elucidated by deconvoluting the Ag 3d and Ti 2p spectra. The deconvoluted Ag 3d spectra (Fig. 2d) comprises two prominent peaks related to Ag $3d_{3/2}$ and Ag $3d_{5/2}$ at the binding energy of 372.9, 366.9 eV, respectively, indicating the direct reduction of silver from Ag^+ to Ag(0) (Pandey et al., 2018). Additionally, the binding energy splitting is obtained 6 eV, demonstrating the presence of metallic AgNPs in the nanohybrid. Similarly, the deconvoluted Ti 2p spectra (Fig. 2e) comprises two main peaks at 458.8 and 464.6 eV related to Ti(iv) $2p_{3/2}$, and Ti(iv) $2p_{1/2,}$ respectively (Zou et al., 2016). The self-reduction process provides the transformation of Ti (iii) and Ti (ii) to the terminated Ti (iv) species (Fig. 2e), validating the successful reduction of $AgNO_3$ to AgNPs by MXene nanosheets. This uniform deposition and self-reduction of AgNPs on Ti_3C_2-MXene nanosheets can be attributed to the activated low valence Ti species in the Ti_3C_2-MXene nanosheets (Pandey et al., 2018).

The detailed surface morphological analysis of synthesized Ti_3C_2-MXene and Ag@Ti_3C_2-MXene nanohybrid are investigated through TEM and FE-SEM characterizations. Stacked MXene flakes having flake sizes around 2–3 μm can be observed in the synthesized bare Ti_3C_2-MXene (Figs. S5–7). However, the Ag@Ti_3C_2-MXene nanohybrid indicates the presence of non-aggregated and uniformly decorated AgNPs on ultrathin Ti_3C_2-MXene nanosheets (Fig. 3a–f). The energy dispersive X-ray spectroscopy (EDS) is also performed for the elemental spectrum, and mapping analysis. The EDS spectrum of Ti_3C_2-MXene (Fig. S3a) exhibits the occurrence of oxygen (O), carbon (C), and titanium (Ti) elements, whereas the spectrum of Ag@Ti_3C_2-MXene nanohybrid (Fig. S3b) reveals the existence of Ag along with O, C, and Ti. These elements are mapped with individual colors viz. yellow (Ag), turquoise (Ti), red (C), and green (O) for Ag@Ti_3C_2-MXene nanohybrid (Fig. 3h); and yellow (Ti), red (C), and green (O) for Ti_3C_2-MXene nanosheets (Fig. S4). Additionally, the line scan analysis is also carried out across the individual sheets, and their corresponding effects are depicted in Fig. S5 and Fig. 3i, which also evident the existence and distribution of these elements.

3.3. *Steady-state and time-resolved spectroscopic studies between anti-NSE/amino-GQDs and Ag@Ti_3C_2-MXene nanohybrid*

An effective energy transfer system requires an extensive selection of donor-acceptor pair that relies on the criteria of overlap between the emission spectra of donor species and absorption spectra of acceptor species (Neema et al., 2020). Herein, an optimal overlap has been obtained for the selected donor-acceptor pair, indicating the plausible energy transfer process (Fig. S8). Compared to previously reported

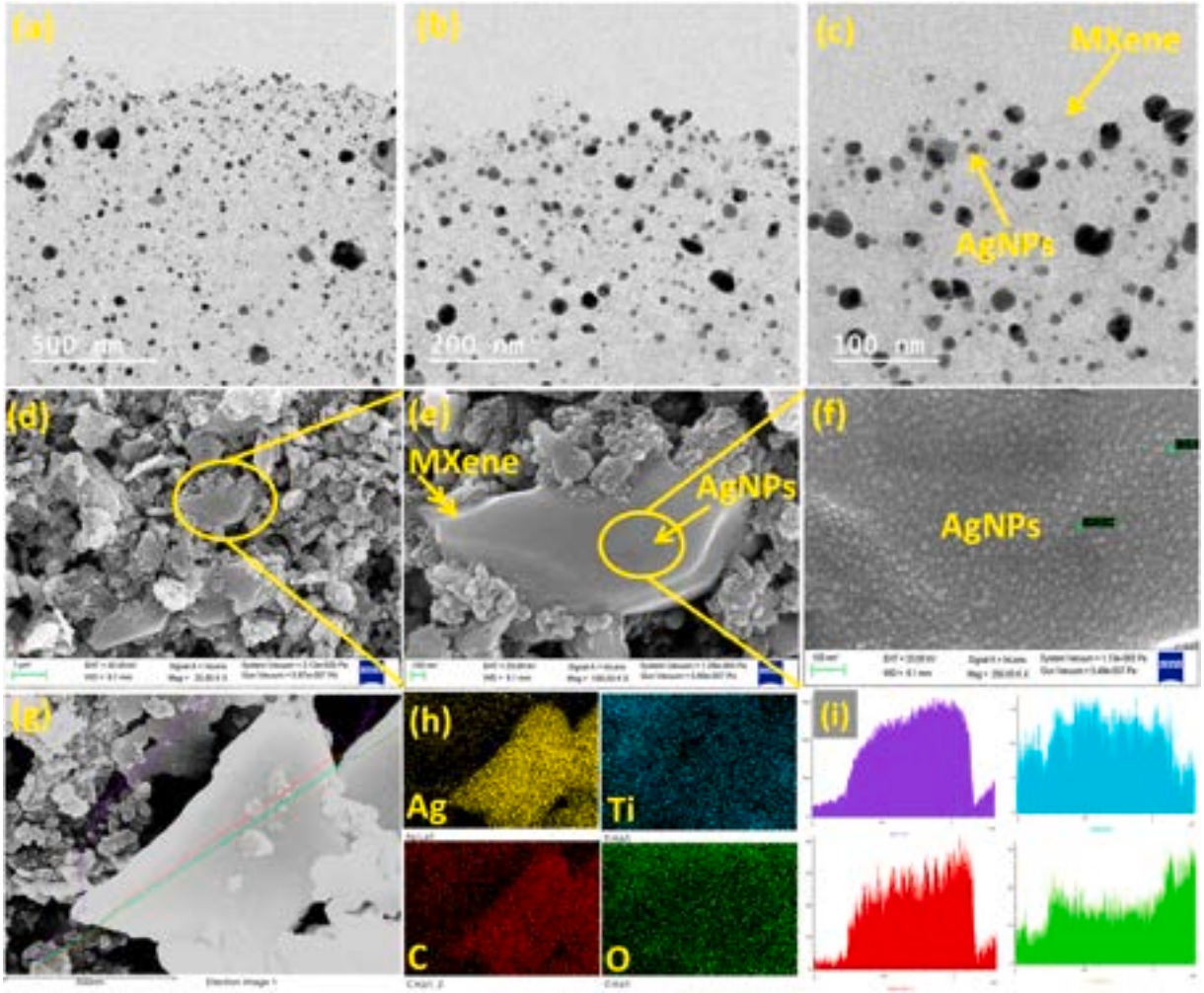

Fig. 3. **(a–c)** TEM images of Ag@Ti_3C_2-MXene nanohybrid at different scales, indicating the decoration of AgNPs on ultrathin Ti_3C_2-MXene nanosheets **(d–g)** FE-SEM images of Ag@Ti_3C_2-MXene nanohybrid at different magnifications; **(h)** Elemental mapping of Ag@Ti_3C_2-MXene nanohybrid revealing the presence of Ag (yellow), Ti (turquoise), C (red), and O (green) elements; **(i)** Line scan analysis of Ag@Ti_3C_2-MXene nanohybrid across the individual sheet. (For interpretation of the references to color in this figure legend, the reader is referred to the Web version of this article.)

AuNPs energy acceptor (Kalkal et al., 2020), the Ag@Ti_3C_2-MXene nanohybrid indicates better spectra overlap, signifying the improved energy transfer kinetics. The fluorescence quenching ability of Ag@Ti_3C_2-MXene nanohybrid has been compared with bare Ti_3C_2-MXene, AgNPs and earlier reported AuNPs. The protein-functionalized amino-GQDs are incubated with increasing concentrations of AgNPs, Ti_3C_2-MXene and Ag@Ti_3C_2-MXene nanohybrid followed by recording their corresponding emission spectra. It has been found that the fluorescence intensity of protein functionalized amino-GQDs decreases progressively after the addition of increasing concentrations of AgNPs (Fig. S9), Ti_3C_2-MXene (Fig. 4a), and Ag@Ti_3C_2-MXene (Fig. 4b) nanohybrid. This quenching can be attributed to the dipole-surface interactions between donor-acceptor pairs. The quenching efficiency (QE) with these materials was determined using **Eq. (S1)** and then compared. It has been observed that the Ag@Ti_3C_2-MXene exhibits higher quenching efficiency (~94%) compared to bare Ti_3C_2-MXene (~87%), AgNPs (~84) and AuNPs (~81%) (Kalkal et al., 2020). This increase in QE might be attributed to the synergistic effect of Ag@Ti_3C_2-MXene nanohybrid, which acts as a dual-quencher in a single system for the ultra-high fluorescence quenching of anti-NSE/amino-GQDs. The higher surface to volume ratio of Ag@Ti_3C_2-MXene nanohybrid may enable efficient fluorescence quenching by introducing the concept of single-acceptor and multiple-donor (as depicted in Fig. 1). The integration of AgNPs to Ti_3C_2-MXene nanosheets offered a stable nanohybrid that may prevent the aggregation and stacking of bare AgNPs and Ti_3C_2-MXene nanosheets, respectively, resulting in enhanced QE.

Subsequently, the Stern-Volmer studies are examined to determine the quenching mechanism (Kumar et al., 2019a, 2020). In this context, Fig. 4d indicates the plots of F_0/F as a function of quencher concentration. The obtained linear plots signify the dynamic nature of quenching with both Ti_3C_2-MXene and Ag@Ti_3C_2-MXene (Swaminathan et al., 2017). Besides, the time-resolved fluorescence spectroscopy is carried out to study the nature of interactive energy transfer between donor-acceptor pair and measure the fluorescence lifetime of the donor in the presence and absence of quencher. Fig. 4e indicates the corresponding spectra of protein functionalized amino-GQDs with increasing Ag@Ti_3C_2-MXene concentrations. After the addition of increased Ag@Ti_3C_2-MXene concentration, the fluorescence lifetime of anti-NSE/amino-GQDs is observed to be progressively reduced, confirming the energy transfer mechanism from the anti-NSE/amino-GQDs

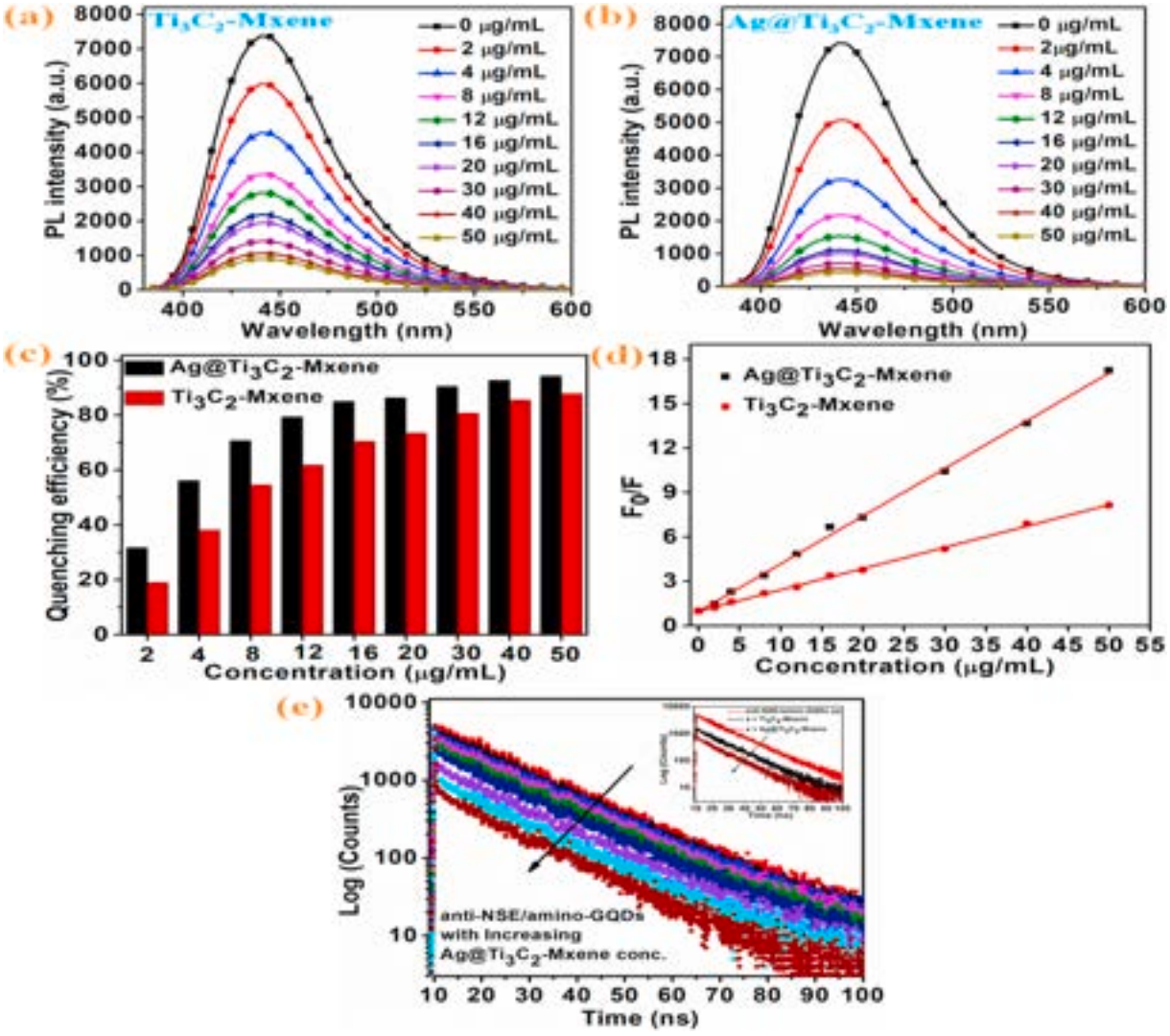

Fig. 4. Steady-state fluorescence quenching spectra of protein functionalized amino-GQDs with escalating concentrations (0–50 µg mL^{-1} from top to bottom, λex = 360 nm, λem ~ 450 nm); **(a)** bare Ti_3C_2-MXene **(b)** Ag@Ti_3C_2-MXene; **(c)** The comparison of fluorescence QE induced by Ti_3C_2-MXene and Ag@Ti_3C_2-MXene; **(d)** Stern-Volmer plot indicating the variation of F_0/F with different concentration of Ti_3C_2-MXene/Ag@Ti_3C_2-MXene from 0 to 50 µg mL^{-1}; **(e)** Time-resolved fluorescence spectra of protein-functionalized amino-GQDs with increasing concentration of Ag@Ti_3C_2-MXene nanohybrid (inset shows the lifetime decay spectra of protein-functionalized amino-GQDs alone and with added Ti_3C_2-MXene and Ag@Ti_3C_2-MXene (200 µL, 0.05 mg mL^{-1}).

to Ag@Ti_3C_2-MXene. In Fig. 4e, the downward inclined arrow states that the dynamics of emission decay become faster when the concentration of Ag@Ti_3C_2-MXene nanohybrid is increased. The protein functionalized amino-GQDs fluorescence lifetime follows bi-exponential decay dynamics with $\tau_1 = 8.04$ ns (fast component), and $\tau_2 = 16.64$ ns (slow component). Upon the addition of Ag@Ti_3C_2-MXene, the τ_1, τ_2 decrease from 8.04 to 2.4 ns and 16.64 to 15.26 ns, respectively. The inset of Fig. 4e indicates the lifetime decay spectra of protein-functionalized amino-GQDs alone and added Ti_3C_2-MXene and Ag@Ti_3C_2-MXene (200 μL, 0.05 mg mL^{-1}). The energy transfer performance of Ag@Ti_3C_2-MXene nanohybrid has been compared with bare Ti_3C_2-MXene and AuNPs (Kalkal et al., 2020), calculated using **Eq. (1)**.

$$\varphi_E = 1 - \frac{\tau_{DA}}{\tau_D} \quad (1)$$

Where τ_{DA} and τ_D are the fluorescence lifetime of protein-functionalized amino-GQDs with and without quencher, respectively. It has been observed that the Ag@Ti_3C_2-MXene exhibits a higher energy transfer efficiency (~70%) compared to bare Ti_3C_2-MXene (~54) and AuNPs (43%) (Kalkal et al., 2020). This increased efficiency can be attributed to the prepared non-aggregated, unstacked, and stable Ag@Ti_3C_2-MXene nanohybrid that might enable faster energy transfer kinetics from the donor species by working as an efficient dual-energy acceptor. The free conduction electrons present in AgNPs can facilitate in providing higher energy accepting capability through dipole vectors on their surface, high molecular extinction coefficient, and larger absorption spectra overlap near the Plasmon resonance frequency (Ghosh and Chattopadhyay, 2015). Furthermore, it is reported that AgNPs lack a defined dipole moment; thereby, energy transfer to AgNPs can occur in any orientation of donor species (Ghosh and Chattopadhyay, 2015; Shi et al., 2015). Apart from that, Ti_3C_2-MXene sheets exhibit wideband absorption in the UV–vis region over its large surface area in conjunction with long-range electron and energy transferability, providing improved energy transfer (Shi et al., 2019; Zhang et al., 2018).

3.4. Analytical performance of the anti-NSE/amino-GQDs/Ag@Ti_3C_2-MXene based fluorescent biosensor

Under optimal conditions (supporting **information (S7), Figs. S10–11**), the fluorescence spectroscopy has been carried out to explore the analytical performance of anti-NSE/amino-GQDs/Ag@Ti_3C_2-MXene (Fig. 5a) and anti-NSE/amino-GQDs/Ti_3C_2-MXene

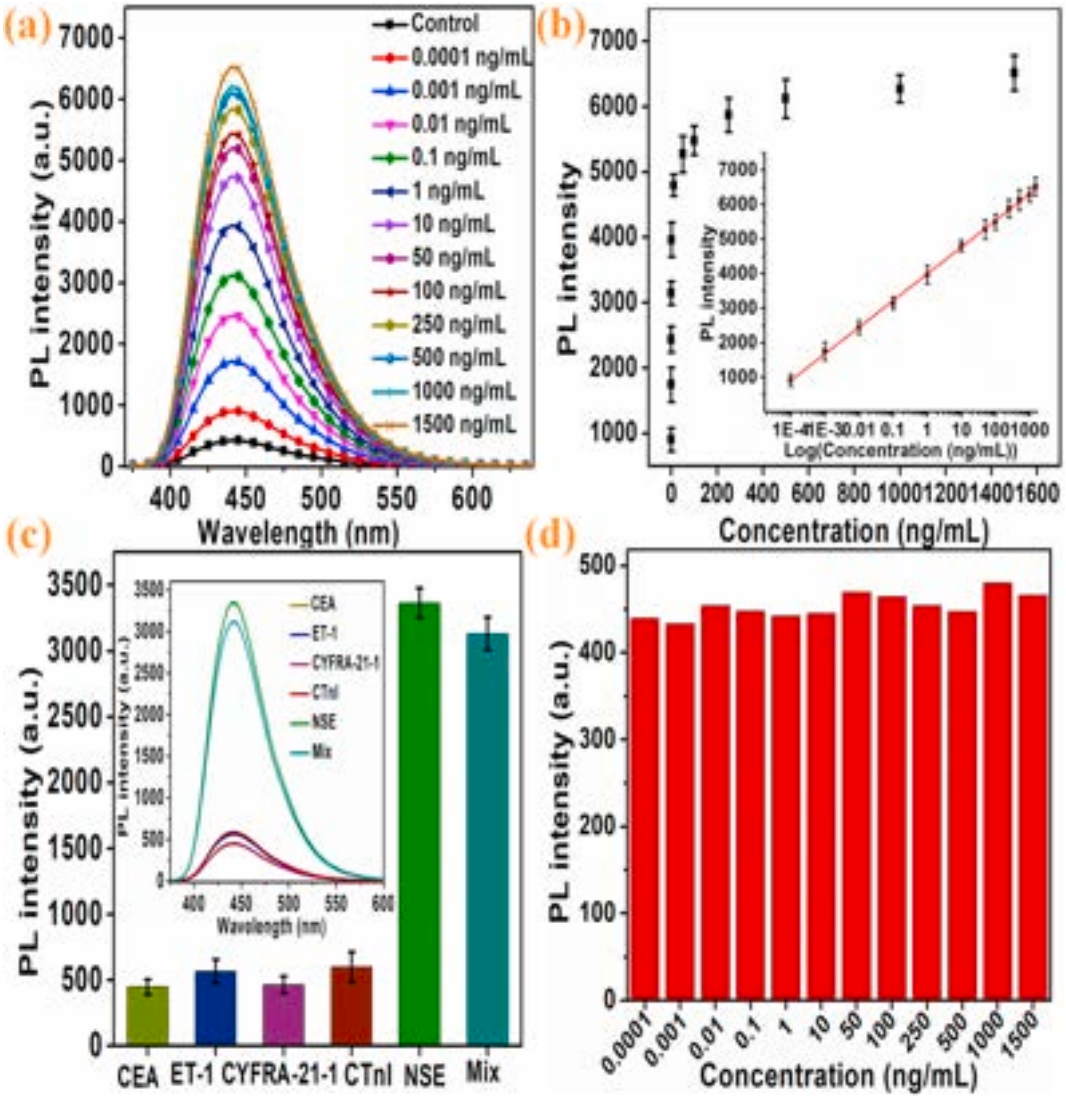

Fig. 5. (a) Analytical performance of the anti-NSE/amino-GQDs/Ag@Ti_3C_2-MXene based fluorescent biosensor toward NSE detection **(b)** Graph between recovered fluorescence and different NSE concentration, Inset indicates the corresponding calibration curve between recovered fluorescence and log NSE concentration in the range of 0.0001–1500 ng mL^{-1} **(c)** Selectivity studies of proposed biosensor **(d)** Control experiment for the amino-GQDs/Ag@Ti_3C_2-MXene immunoelectrode.

(Fig. S12) based fluorescent immunosensing platforms toward different concentrations (0.0001–1500 ng mL^{-1}) of NSE. It has been found that the fluorescence intensity of protein functionalized amino-GQDs restore with increasing NSE antigen concentration. The restoration in the fluorescence intensity is linearly correlated to the added concentration and can be ascribed to the formation of the antigen-antibody immunocomplex (Chen et al., 2018; Das et al., 2018). For each added concentration, the formed complex increases the distance among donor-acceptor species. Consequently, there will be no energy transfer from the protein-functionalized amino-GQDs to the Ag@Ti_3C_2-MXene/Ti_3C_2-MXene, and hence the fluorescence intensity starts to restore gradually. Fig. 5b and Fig. S12d indicate the calibration plot between recovered fluorescence intensities and log NSE concentration for anti-NSE/amino-GQDs/Ag@Ti_3C_2-MXene and anti-NSE/amino-GQDs/Ti_3C_2-MXene, respectively. In case of anti-NSE/amino-GQDs/Ag@Ti_3C_2-MXene, an established linear correlation is obtained in the dynamic range of 0.0001–1500 ng mL^{-1}, described by the linear regression equation **Eq. (2)**. Whereas, in case of anti-NSE/amino-GQDs/Ti_3C_2-MXene, a linear correlation is obtained in the range of 1–1000 ng mL^{-1}, described by **Eq. (S2)**.

$$I = 771.54 \log_{10} NSE \ \ (ng \ \ mL^{-1}) + 3987.04, \text{ the Regression coefficient } R^2 = 0.99 \quad (2)$$

Further, the limit of detection (LOD) is calculated according to the standard equation (**Eq. S3**). The LOD for anti-NSE/amino-GQDs/Ag@Ti_3C_2-MXene and anti-NSE/amino-GQDs/Ti_3C_2-MXene immunoprobes is calculated as 0.05 pg mL^{-1} and 0.34 ng mL^{-1}, respectively. Besides, we have compared the analytical performance of anti-NSE/amino-GQDs/Ag@Ti_3C_2-MXene fluorescent biosensor with classic 2D graphene (Fig. S13) and our previously reported AuNPs based sensing platforms. It is found that the anti-NSE/amino-GQDs/Ag@Ti_3C_2-MXene based biosensing platform exhibits better LOD, broader linear detection range, improved sensitivity, and a faster response time. Specifically, the sensitivity of Ag@Ti_3C_2-MXene based platform (~771 mL ng^{-1}) is exceeding two times in contrast to graphene (~352 mL ng^{-1}) as well as AuNPs (~333 mL ng^{-1}) (Kalkal et al., 2020) based platforms. Furthermore, the biosensing characteristics of the present fluorescent biosensor are summarized in Table 1, along with reported aptasensors, sandwich assays, and immunosensors for NSE detection.

3.5. Selectivity of the proposed fluorescent biosensor

The developed fluorescent biosensor has been found to exhibit good performance toward the detection of NSE biomarker. However, in human serum, various interfering biomarkers (other than NSE) such as cytokeratin-19 fragment (CYFRA-21-1), cardiac troponin-I (cTnI), endothelin-1 (ET-1), carcinoembryonic antigen (CEA) are also present. These interfering biomarkers may also contribute towards the fluorescence recovery of the fabricated biosensor. Therefore, it becomes crucial to examine the efficacy of developed biosensor in the presence of these potential serum biomarkers. In this context, Fig. 5c indicates the response of the biosensor in the presence of individual cancer biomarker (50 μL, 0.1 ng mL^{-1}) and mixture of all biomarkers. A marginal recovery in fluorescence has been observed with interfering cancer biomarkers. The fluorescence recovery difference is estimated to be less than 5% when compared to the blank sample (anti-NSE/amino-GQDs/Ag@Ti_3C_2-MXene). Additionally, the selectivity coefficient (SC) is also determined for each biomarker utilizing **Eq. (S5)** and found to be ~1. In addition, the corresponding analytical signal is recorded to examine the selectivity of the immunosensor in a mixture of NSE and other mentioned biomarkers, which commensurate with the analytical signal linked to NSE alone, as shown in Fig. 5c. These findings explicitly suggest that fluorescence recovery is caused by specific NSE biomarker, demonstrating the excellent selectivity of the proposed fluorescent biosensor for NSE detection.

3.6. Control and reproducibility studies

Under similar conditions, the fluorescence response of the amino-GQDs/Ag@Ti_3C_2-MXene has been recorded in the same range (0.0001–1500 ng mL^{-1}) as a controlled sample for NSE detection. The findings obtained (Fig. 5d) reveal that there is no substantial restoration of the fluorescence intensity against the added NSE concentration, suggesting that the restoration of fluorescence intensity is primarily due to the unique antibody-antigen interactions. Besides, fluorescent immunosensor reproducibility (Fig. S14) is determined by identifying NSE (50 μL, 1 ng mL^{-1}) using five distinctive fluorescent probes fabricated under comparable conditions. The measured relative standard deviation of less than 10 percent (% RSD) signifies higher reproducibility and good accuracy.

Table 1
Analytical comparison of anti-NSE/amino-GQDs/Ag@Ti_3C_2-MXene based biosensor with earlier reported biosensing platforms for NSE detection.

Sr. No.	Analytical Platform	Technique	Linear range (ng mL^{-1})	Limit of detection	Sensitivity	Time (min)	Ref.
1.	NH2-G/Thi/AuNPs POCT	Differntial pulse Voltametry (DPV)	1–500	10 pg mL^{-1}	0.941 μA mL ng−1	18	Fan et al. (2017)
2.	MB-COOH/NH2-Apt-5	Chemiluminescence (CL)	1–100	0.1 ng mL^{-1}	26.34 mL ng−1	–	Zheng et al. (2019)
3.	Fc-g-Au@Pd–P(BBY) and rGO/Thi/AuPt NAs	Electrochemical Impedance spectroscopy (EIS)	0.0001–50.0	0.03 pg mL^{-1}	–	–	Chen et al. (2020)
4.	anti-NSE/DA/TiO_2/FTO	Photocurrent	0.1–1000	0.05 ng mL^{-1}	–	30	Li et al. (2017)
5.	CEA/anti-CEA/CNTs-AuNPs/GCE	Cyclic Voltametry (CV)	0.10–200	0.04 ng mL^{-1}	1.56 μA mL ng−1	20	Gao et al. (2011)
6.	FITC-anti-NSE/ALP-NSE/anti-FITC-MB	CL	0–300	0.2 ng mL^{-1}	4774.8 mL ng−1	–	Fu et al. (2012)
7.	ITO/NiWO4/Ab	Photocurrent	75–723	0.12 ng mL^{-1}	–	–	Soomro et al. (2019)
8.	HRP-P4/anti-P4/GCE	chronoamperometry	0.50–12.5	0.20 ng mL^{-1}	3.0 ± 0.1 nA ng−1 mL	15	Arévalo et al. (2010)
9.	anti-NSE/Au–Gra/NiHCFNPs/AuNCs/GCE	CV	0.001–100	0.3 pg mL^{-1}	60.84 μA mL ng−1	30	Han et al. (2012)
10.	anti-NSE/amine-N-GQDs @AuNPs	Fluorescence Spectroscopy (FS)	0.0001–1000	0.09 pg mL^{-1}	333.20 mL ng−1	16	Kalkal et al. (2020)
11.	**anti-NSE/amino-GQDs/Ti_3C_2-MXene**	FS	1–1000	0.34 ng mL^{-1}	875.57 mL ng−1	–	**This work**
12.	**anti-NSE/amino-GQDs/Ag@$T_{i3}C_2$-MXene**	FS	**0.0001–1500**	**0.05 pg mL^{-1}**	771.54 mL ng−1	**12**	**This work**

3.7. Real sample analysis

For real sample analysis, the collected serum samples are spiked with 50 μL of known NSE antigen concentrations (10, 20, 50, 100, and 150 ng mL^{-1}). Fig. S15a shows the results of the proposed immunosensor (anti-NSE/amino-GQDs/Ag@Ti_3C_2-MXene) toward five different NSE spiked serum samples. The incubation time of 12 min is provided for having the immunoreaction (antigen-antibody interactions) as in the previous experiment. For both the standard and spiked serum samples, a strong correlation suggesting a similar pattern of fluorescence intensity recovery has been obtained. The calibration plot between the fluorescence intensities and log of target biomarker concentration has been depicted in Fig. S15b. A linear relation has been realized, described by **Eq. (S6)**. The % recovery in the spiked serum samples is determined using **Eq. (3)** and listed in Table S1.

$$\%\ \text{recovery} = \frac{yi - yo}{ys} \times 100 \tag{3}$$

Where y_s is the actual NSE spiked concentration and y_i, y_o are the obtained concentrations in spiked and unspiked samples, respectively. The anti-NSE/amino-GQDs/Ag@Ti_3C_2-MXene based fluorescent immunosensor exhibit an average recovery of ~98%. The obtained results signify that the fabricated immunosensor can quantitatively detect the NSE biomarker in the clinical samples.

4. Conclusions

In the present work, a potential fluorescent biosensor comprised of biofunctionalized graphene quantum dots and Ag@Ti_3C_2-MXene nanohybrid is developed for the quantitative NSE detection. The functionality of this selective, rapid, label-free, and highly sensitive biosensor relies on the fluorescence quenching of donor species (anti-NSE/amino-GQDs) by the acceptor species (Ag@Ti_3C_2-MXene), followed by the restoration of quenched fluorescence upon the addition of NSE antigen. The Ag@Ti_3C_2-MXene nanohybrid as dual-energy acceptor exhibits higher quenching efficiency (~94%) compared to bare Ti_3C_2-MXene (~87%), AgNPs (~84%) and earlier reported AuNPs (~81%). Simultaneously, the energy transfer efficiency improved to 70% compared to Ti_3C_2-MXene (54%), and AuNPs (43%). Moreover, the developed Ag@Ti_3C_2-MXene nanohybrid-based biosensor exhibit improved biosensing parameters such as broader linear detection range (0.0001–1500 ng mL^{-1}), better LOD (0.05 pg mL^{-1}), higher sensitivity (~771 mL ng^{-1}), and faster response time (12 min). It is worth mentioning that the sensitivity of Ag@Ti_3C_2-MXene based biosensing platform is exceeding two times in contrast to classic graphene (~352 mL ng^{-1}) and our earlier reported AuNPs (~333 mL ng^{-1}) based platforms. On the other hand, enhanced linear detection range and LOD are observed in contrast to bare Ti_3C_2-MXene and graphene. The present biosensor also reveals remarkable performance in serum samples with ~98% average spiked NSE restoration. In nutshell, the developed immunosensor exhibits remarkable biosensing characteristics that make it a promising platform for quantitative NSE detection. Further efforts should be made towards integrating this potential platform with microfluidics and flexible electronics in creating the miniaturized point-of-care device.

Declaration of competing interest

The authors declare that they have no known competing financial interests or personal relationships that could have appeared to influence the work reported in this paper.

Acknowledgments

The present work is supported by the Department of Biotechnology (No. BT/PR25095/NER/95/1011/2017) Government of India. A. Kalkal and S. Kadian are grateful to the Ministry of Education, India for the fellowship and Microfluidic Devices & Heterogeneous Systems Lab, Centre for Nano Science and Engineering (CeNSE), IISc, Bengaluru, India for the Internship. P. Gopinath would like to thank the Department of Science and Technology (DST), Government of India, Technology Innovation Hub (TIH) [A Section-8 Company: Divyasampark]. Saurabh Kumar acknowledges the DST for the DST-INSPIRE Faculty Award (DST/INSPIRE/04/2017/002750). Authors are thankful to the Centre of Nanotechnology, Department of Biosciences and Bioengineering IIT Roorkee and CeNSE, IISc, Bengaluru, India, for providing the required infrastructure and various characterization facilities.

Appendix A. Supplementary data

Supplementary data to this article can be found online at https://doi.org/10.1016/j.bios.2021.113620.

Author contributions

Ashish Kalkal, Saurabh kumar and P. Gopinath conceptualized the work. P. Gopinath, Saurabh Kumar, Prosenjit Sen, and Sumit Kumar provided valuable inputs and edited the manuscript. Ti_3C_2-MXene, Ag@Ti_3C_2-MXene nanohybrid synthesis, and optimization were carried out at CeNSE, IISc Bengaluru. Ti_3C_2-MXene and Ag@Ti_3C_2-MXene nanohybrid characterizations, biosensor fabrication, optimization, analysis and manuscript writing were performed by Ashish Kalkal. Sachin Kadian and Gaurav Manik provided their input in the XRD, UV, XPS, and PL characterizations. Sumit Kumar provided his input in performing the lifetime spectra. All authors contributed to draft the manuscript.

References

Amani, J., Maleki, M., Khoshroo, A., Sobhani-Nasab, A., Rahimi-Nasrabadi, M., 2018. An electrochemical immunosensor based on poly p-phenylenediamine and graphene nanocomposite for detection of neuron-specific enolase via electrochemically amplified detection. Anal. Biochem. 548, 53–59.

Amjadi, M., Abolghasemi-Fakhri, Z., Hallaj, T., 2015. Carbon dots-silver nanoparticles fluorescence resonance energy transfer system as a novel turn-on fluorescent probe for selective determination of cysteine. J. Photochem. Photobiol. Chem. 309, 8–14.

Anasori, B., Lukatskaya, M.R., Gogotsi, Y., 2017. 2D metal carbides and nitrides (MXenes) for energy storage. Nature Reviews Materials 2 (2), 16098.

Arévalo, F.J., Messina, G.A., Molina, P.G., Zón, M.A., Raba, J., Fernández, H., 2010. Determination of progesterone (P4) from bovine serum samples using a microfluidic immunosensor system. Talanta 80 (5), 1986–1992.

Atif, R., Inam, F., 2016. Reasons and remedies for the agglomeration of multilayered graphene and carbon nanotubes in polymers. Beilstein J. Nanotechnol. 7, 1174–1196.

Bellunato, A., ArjmandiTash, H., Cesa, Y., Schneider, G.F., 2016. Chemistry at the Edge of Graphene 17 (6), 785–801.

Bhatnagar, D., Kumar, V., Kumar, A., Kaur, I., 2016. Graphene quantum dots FRET based sensor for early detection of heart attack in human. Biosens. Bioelectron. 79, 495–499.

Cha, J., Kyoung, W., Song, K., Park, S., Lim, T., Lee, J., Kang, H., 2016. Quantitative evaluation of the dispersion of graphene sheets with and without functional groups using molecular dynamics simulations. Nanoscale research letters 11 (1), 136-136.

Chauhan, D., Pooja, Nirbhaya, V., Srivastava, C.M., Chandra, R., Kumar, S., 2020. Nanostructured transition metal chalcogenide embedded on reduced graphene oxide based highly efficient biosensor for cardiovascular disease detection. Microchem. J. 155, 104697.

Chen, B., Su, Q., Kong, W., Wang, Y., Shi, P., Wang, F., 2018. Energy transfer-based biodetection using optical nanomaterials. J. Mater. Chem. B 6 (19), 2924–2944.

Chen, Y., Ge, X.-Y., Cen, S.-Y., Wang, A.-J., Luo, X., Feng, J.-J., 2020. Ultrasensitive dual-signal ratiometric electrochemical aptasensor for neuron-specific enolase based on Au nanoparticles@Pd nanoclusters-poly(bismarck brown Y) and dendritic AuPt nanoassemblies. Sensor. Actuator. B Chem. 311, 127931.

Cui, S., Mao, S., Wen, Z., Chang, J., Zhang, Y., Chen, J., 2013. Controllable synthesis of silver nanoparticle-decorated reduced graphene oxide hybrids for ammonia detection. Analyst 138 (10), 2877–2882.

Das, P., Sedighi, A., Krull, U.J., 2018. Cancer biomarker determination by resonance energy transfer using functional fluorescent nanoprobes. Anal. Chim. Acta 1041, 1–24.

Fan, Y., Liu, J., Wang, Y., Luo, J., Xu, H., Xu, S., Cai, X., 2017. A wireless point-of-care testing system for the detection of neuron-specific enolase with microfluidic paper-based analytical devices. Biosens. Bioelectron. 95, 60–66.

Fu, X., Meng, M., Zhang, Y., Yin, Y., Zhang, X., Xi, R., 2012. Chemiluminescence enzyme immunoassay using magnetic nanoparticles for detection of neuron specific enolase in human serum. Anal. Chim. Acta 722, 114–118.
Gao, X., Zhang, Y., Wu, Q., Chen, H., Chen, Z., Lin, X., 2011. One step electrochemically deposited nanocomposite film of chitosan–carbon nanotubes–gold nanoparticles for carcinoembryonic antigen immunosensor application. Talanta 85 (4), 1980–1985.
Ghidiu, M., Naguib, M., Shi, C., Mashtalir, O., Pan, L.M., Zhang, B., Yang, J., Gogotsi, Y., Billinge, S.J.L., Barsoum, M.W., 2014. Synthesis and characterization of two-dimensional Nb4C3 (MXene). Chem. Commun. 50 (67), 9517–9520.
Ghosh, D., Chattopadhyay, N., 2015. Gold and silver nanoparticles based superquenching of fluorescence: a review. J. Lumin. 160, 223–232.
Han, J., Zhuo, Y., Chai, Y.-Q., Yuan, Y.-L., Yuan, R., 2012. Novel electrochemical catalysis as signal amplified strategy for label-free detection of neuron-specific enolase. Biosens. Bioelectron. 31 (1), 399–405.
Harding, M., McAllister, J., Hulks, G., Vernon, D., Monie, R., Paul, J., Kaye, S.B., 1990. Neurone specific enolase (NSE) in small cell lung cancer: a tumour marker of prognostic significance? Br. J. Canc. 61 (4), 605–607.
He, X., Zhang, S., Pan, H., Chen, J., Xu, J., 2019. Horizontally aggregation of monolayer reduced graphene oxide under deep UV irradiation in solution. Nanoscale Research Letters 14 (1), 117.
Huang, K., Li, Z., Lin, J., Han, G., Huang, P., 2018. Two-dimensional transition metal carbides and nitrides (MXenes) for biomedical applications. Chem. Soc. Rev. 47 (14), 5109–5124.
Ikram, M., Raza, A., Imran, M., Ul-Hamid, A., Shahbaz, A., Ali, S., 2020. Hydrothermal synthesis of silver decorated reduced graphene oxide (rGO) nanoflakes with effective photocatalytic activity for wastewater treatment. Nanoscale Research Letters 15 (1), 95.
Jackman, D.M., Johnson, B.E., 2005. Small-cell lung cancer. Lancet 366 (9494), 1385–1396.
Kadian, S., Manik, G., Kalkal, A., Singh, M., Chauhan, R.P., 2019. Effect of sulfur doping on fluorescence and quantum yield of graphene quantum dots: an experimental and theoretical investigation. Nanotechnology 30 (43), 435704.
Kalali, E.N., Guo, W., Wang, X., Xing, W., Song, L., Hu, Y., 2020. Effect of metal-based nanoparticles decorated graphene hybrids on flammability of epoxy nanocomposites. Compos. Appl. Sci. Manuf. 129, 105694.
Kalkal, A., Allawadhi, P., Pradhan, R., Khurana, A., Bharani, K.K., Packirisamy, G., 2021a. Allium sativum derived carbon dots as a potential theranostic agent to combat the COVID-19 crisis. Sensors International 2, 100102.
Kalkal, A., Kadian, S., Pradhan, R., Manik, G., Packirisamy, G., 2021b. Recent advances in graphene quantum dot-based optical and electrochemical (bio)analytical sensors. Materials Advances 2 (17), 5513–5541.
Kalkal, A., Kumar, S., Kumar, P., Pradhan, R., Willander, M., Packirisamy, G., Kumar, S., Malhotra, B.D., 2021c. Recent advances in 3D printing technologies for wearable (bio)sensors. Additive Manufacturing 46, 102088.
Kalkal, A., Pradhan, R., Kadian, S., Manik, G., Packirisamy, G., 2020. Biofunctionalized graphene quantum dots based fluorescent biosensor toward efficient detection of small cell lung cancer. ACS Applied Bio Materials 3 (8), 4922–4932.
Khazaei, M., Arai, M., Sasaki, T., Chung, C.-Y., Venkataramanan, N.S., Estili, M., Sakka, Y., Kawazoe, Y., 2013. Novel electronic and magnetic properties of two-dimensional transition metal carbides and nitrides. Adv. Funct. Mater. 23 (17), 2185–2192.
Kumar, S., Ashish, Kumar, S., Augustine, S., Yadav, S., Yadav, B.K., Chauhan, R.P., Dewan, A.K., Malhotra, B.D., 2018a. Effect of Brownian motion on reduced agglomeration of nanostructured metal oxide towards development of efficient cancer biosensor. Biosens. Bioelectron. 102, 247–255.
Kumar, S., Kalkal, A., 2021. 3 - electrochemical detection: cyclic voltammetry/differential pulse voltammetry/impedance spectroscopy. In: Khondakar, K.R., Kaushik, A.K. (Eds.), Nanotechnology in Cancer Management. Elsevier, pp. 43–71.
Kumar, S., Kumar, J., Narayan Sharma, S., Srivastava, S., 2019a. rGO integrated MEHPPV and P3HT polymer blends for bulk hetero junction solar cells: a comparative insight. Optik 178, 411–421.
Kumar, Sumit, Sharma, Shailesh N., Kumar, Jitendra, 2019b. Comparative charge transport study of MEHPPV-TiO2 and P3HT-TiO2 nanocomposites for hybrid bulk heterojunction solar cells. J. Nanosci. Nanotechnol. 6, 3408–3419. https://doi.org/10.1166/jnn.2019.16130.
Kumar, S., Kumar, J., Sharma, S.N., 2020. Investigation of charge transfer properties in MEHPVV and rGO-AA nanocomposites for Green organic photovoltaic application. Optik 208, 164540.
Kumar, S., Lei, Y., Alshareef, N.H., Quevedo-Lopez, M.A., Salama, K.N., 2018b. Biofunctionalized two-dimensional Ti3C2 MXenes for ultrasensitive detection of cancer biomarker. Biosens. Bioelectron. 121, 243–249.
Kumar, S., Sharma, J.G., Maji, S., Malhotra, B.D., 2016. Nanostructured zirconia decorated reduced graphene oxide based efficient biosensing platform for non-invasive oral cancer detection. Biosens. Bioelectron. 78, 497–504.
Li, H., Xiao, Q., Lv, J., Lei, Q., Huang, Y., 2017. Dopamine modified hyperbranched TiO2 arrays based ultrasensitive photoelectrochemical immunosensor for detecting neuron specific enolase. Anal. Biochem. 531, 48–55.
Liu, G., Zou, J., Tang, Q., Yang, X., Zhang, Y., Zhang, Q., Huang, W., Chen, P., Shao, J., Dong, X., 2017. Surface modified Ti3C2 MXene nanosheets for tumor targeting photothermal/photodynamic/chemo synergistic therapy. ACS Appl. Mater. Interfaces 9 (46), 40077–40086.
Mahdavi, M., Sharifpur, M., Ahmadi, M.H., Meyer, J.P., 2019. Aggregation study of Brownian nanoparticles in convective phenomena. J. Therm. Anal. Calorim. 135 (1), 111–121.
Naguib, M., Kurtoglu, M., Presser, V., Lu, J., Niu, J., Heon, M., Hultman, L., Gogotsi, Y., Barsoum, M.W., 2011. Two-dimensional nanocrystals produced by exfoliation of Ti3AlC2. Adv. Mater. 23 (37), 4248–4253.
Neema, P.M., Tomy, A.M., Cyriac, J., 2020. Chemical sensor platforms based on fluorescence resonance energy transfer (FRET) and 2D materials. Trac. Trends Anal. Chem. 124, 115797.
Pandey, R.P., Rasool, K., Madhavan, V.E., Aïssa, B., Gogotsi, Y., Mahmoud, K.A., 2018. Ultrahigh-flux and fouling-resistant membranes based on layered silver/MXene (Ti3C2Tx) nanosheets. J. Mater. Chem. 6 (8), 3522–3533.
Peng, C., Yang, X., Li, Y., Yu, H., Wang, H., Peng, F., 2016. Hybrids of two-dimensional Ti3C2 and TiO2 exposing {001} facets toward enhanced photocatalytic activity. ACS Appl. Mater. Interfaces 8 (9), 6051–6060.
Peng, X., Zhang, Y., Lu, D., Guo, Y., Guo, S., 2019. Ultrathin Ti3C2 nanosheets based "off-on" fluorescent nanoprobe for rapid and sensitive detection of HPV infection. Sensor. Actuator. B Chem. 286, 222–229.
Pradhan, R., Kalkal, A., Jindal, S., Packirisamy, G., Manhas, S., 2021a. Four electrode-based impedimetric biosensors for evaluating cytotoxicity of tamoxifen on cervical cancer cells. RSC Adv. 11 (2), 798–806.
Pradhan, R., Raisa, S.A., Kumar, P., Kalkal, A., Kumar, N., Packirisamy, G., Manhas, S., 2021b. Optimization, fabrication, and characterization of four electrode-based sensors for blood impedance measurement. Biomed. Microdevices 23 (1), 9.
Rudin, C.M., Brambilla, E., Faivre-Finn, C., Sage, J., 2021. Small-cell lung cancer. Nature Reviews Disease Primers 7 (1), 3.
Shao, K., Wang, L., Wen, Y., Wang, T., Teng, Y., Shen, Z., Pan, Z., 2019. Near-infrared carbon dots-based fluorescence turn on aptasensor for determination of carcinoembryonic antigen in pleural effusion. Anal. Chim. Acta 1068, 52–59.
Shi, J., Tian, F., Lyu, J., Yang, M., 2015. Nanoparticle based fluorescence resonance energy transfer (FRET) for biosensing applications. J. Mater. Chem. B 3 (35), 6989–7005.
Shi, Y.-e., Han, F., Xie, L., Zhang, C., Li, T., Wang, H., Lai, W.-F., Luo, S., Wei, W., Wang, Z., Huang, Y., 2019. A MXene of type Ti3C2Tx functionalized with copper nanoclusters for the fluorometric determination of glutathione. Microchimica Acta 187 (1), 38.
Shibayama, T., Ueoka, H., Nishii, K., Kiura, K., Tabata, M., Miyatake, K., Kitajima, T., Harada, M., 2001. Complementary roles of pro-gastrin-releasing peptide (ProGRP) and neuron specific enolase (NSE) in diagnosis and prognosis of small-cell lung cancer (SCLC). Lung Canc. 32 (1), 61–69.
Song, Q., Ye, F., Kong, L., Shen, Q., Han, L., Feng, L., Yu, G., Pan, Y., Li, H., 2020. Graphene and MXene nanomaterials. Toward High-Performance Electromagnetic Wave Absorption in Gigahertz Band Range 30 (31), 2000475.
Soomro, R.A., Jawaid, S., Zhu, Q., Abbas, Z., Xu, B., 2020. A mini-review on MXenes as versatile substrate for advanced sensors. Chin. Chem. Lett. 31 (4), 922–930.
Soomro, R.A., Kalwar, N.H., Avci, A., Pehlivan, E., Hallam, K.R., Willander, M., 2019. In-situ growth of NiWO4 saw-blade-like nanostructures and their application in photo-electrochemical (PEC) immunosensor system designed for the detection of neuron-specific enolase. Biosens. Bioelectron. 141, 111331.
Su, H., Zhang, C., Li, X., Wu, L., Chen, Y., 2018. Aggregation prevention: reduction of graphene oxide in mixed medium of alkylphenol polyoxyethylene (7) ether and 2-methoxyethanol. RSC Adv. 8 (68), 39140–39148.
Sun, Y., Chen, D., Liang, Z., 2017. Two-dimensional MXenes for energy storage and conversion applications. Materials Today Energy 5, 22–36.
Swaminathan, H., Ramar, V., Balasubramanian, K., 2017. Excited-state electron and energy transfer dynamics between 2D MoS2 and GO/RGO for turn ON BSA/HSA sensing. J. Phys. Chem. C 121 (23), 12585–12592.
Tian, F., Lyu, J., Shi, J., Yang, M., 2017. Graphene and graphene-like two-denominational materials based fluorescence resonance energy transfer (FRET) assays for biological applications. Biosens. Bioelectron. 89, 123–135.
Tilaki, R.M., Iraji zad, A., Mahdavi, S.M., 2006. Stability, size and optical properties of silver nanoparticles prepared by laser ablation in different carrier media. Appl. Phys. A 84 (1), 215–219.
Torres-Mendieta, R., Ventura-Espinosa, D., Sabater, S., Lancis, J., Mínguez-Vega, G., Mata, J.A., 2016. In situ decoration of graphene sheets with gold nanoparticles synthetized by pulsed laser ablation in liquids. Sci. Rep. 6 (1), 30478.
Vedala, H., Sorescu, D.C., Kotchey, G.P., Star, A., 2011. Chemical sensitivity of graphene edges decorated with metal nanoparticles. Nano Lett. 11 (6), 2342–2347.
Xiao, K., Wang, K., Qin, W., Hou, Y., Lu, W., Xu, H., Wo, Y., Cui, D., 2017. Use of quantum dot beads-labeled monoclonal antibody to improve the sensitivity of a quantitative and simultaneous immunochromatographic assay for neuron specific enolase and carcinoembryonic antigen. Talanta 164, 463–469.
Zhang, Q., Wang, F., Zhang, H., Zhang, Y., Liu, M., Liu, Y., 2018. Universal Ti3C2 MXenes based self-standard ratiometric fluorescence resonance energy transfer platform for highly sensitive detection of exosomes. Anal. Chem. 90 (21), 12737–12744.
Zheng, Y., Zhao, Y., Di, Y., He, L., Liao, S., Li, D., Liu, X., 2019. In vitro selection of DNA aptamers for the development of chemiluminescence aptasensor for neuron-specific enolase (NSE) detection. RSC Adv. 9 (27), 15513–15520.
Zhou, H., Wu, F., Fang, L., Hu, J., Luo, H., Guan, T., Hu, B., Zhou, M., 2020. Layered NiFe-LDH/MXene nanocomposite electrode for high-performance supercapacitor. Int. J. Hydrogen Energy 45 (23), 13080–13089.
Zhu, X., Pang, X., Zhang, Y., Yao, S., 2019. Titanium carbide MXenes combined with red-emitting carbon dots as a unique turn-on fluorescent nanosensor for label-free determination of glucose. J. Mater. Chem. B 7 (48), 7729–7735.
Zou, G., Zhang, Z., Guo, J., Liu, B., Zhang, Q., Fernandez, C., Peng, Q., 2016. Synthesis of MXene/Ag composites for extraordinary long cycle lifetime lithium storage at high rates. ACS Appl. Mater. Interfaces 8 (34), 22280–22286.